

Date of publication xxxx 00, 0000, date of current version xxxx 00, 0000.

Digital Object Identifier 10.1109/ACCESS.2020.DOI

Modeling and Experimental Characterization of an Electromagnetic Energy Harvester for Wearable and Biomedical Applications

G. DIGREGORIO¹, H. PIERRE², P. LAURENT³ AND J.-M. REDOUTÉ⁴, (Senior Member, IEEE)

^{1,2,3,4}Department of Electrical Engineering and Computer Science at the University of Liège, Belgium. (e-mail: gabriel.digregorio@uliege.be)

Corresponding author: G. Digregorio (e-mail: gabriel.digregorio@uliege.be).

ABSTRACT This work presents the modeling and the experimental validation of a linear electromagnetic energy harvester (EMEH) actuated by random low-g external acceleration or by a very slow imposed movement. By combining these two different ways of energy scavenging, the system is particularly suited for powering wearable and biomedical electronic devices where the human-motion and movement can be considered as random and non predictable. The design is composed of a mobile stack of head-to-head ring-shaped permanent magnets in which a fixed wounded ferromagnetic core, composed of two coils, is located. A custom co-simulation is presented: a finite element analysis (FEA) and a one dimension (1D) two degrees of freedom (2DOF) system model. The FEA is used to optimize the geometry of the EMEH and its form factor, allowing a significative down-scaling. The 1D 2DOF model describes the dynamics of the EMEH in its real environment by considering all the leading mechanical and electrical parameters. The geometry can drastically change the behavior of the system as well as its dynamics: the goal of this double structure is to reduce the magnetic force exerted between the fixed part and the moving part while keeping the magnetic flux gradient in each coil as large as possible. This force was characterized experimentally by using a custom designed test bench, to validate the FEA results. It was observed that the maximum produced energy is reached when the system sweeps across different equilibrium positions rather than oscillating around a given stable position. The second degree of freedom helps the system to settle in a large number of equilibrium positions when submitted to random external accelerations and therefore broadens the frequency response of the EH. Results show a theoretical electrical power output (RMS) of 2 mW for a 10 cm³ cylindrical harvester submitted to a short external acceleration pulse of 27.5 m/s².

INDEX TERMS Axisymmetrical geometry, eddy currents, electromagnetic energy harvesters, energy harvesting characterization, finite element analysis, magnetic force, two degrees of freedom.

I. INTRODUCTION

ELECTROMAGNETIC energy harvesters (EMEH), capable of generating electrical power from mechanical movement, are actively researched since a few decades to supply low-power electronics such as wireless monitoring devices and sensors for various applications [1]–[5]. They are also intensively investigated in the field of biomedical applications to power various wearable electronics by using human-motion EH [6]–[8] as well as for bio-implantable systems for the harvesting capability of the human heart and diaphragm [9], [10]. The minimum required power to monitor physiological parameters and transmit data wire-

lessly at low rate is in the range of 500 μW [11] [12]. The human body includes various areas where EMEHs can be used to harvest energy [13]. For each harvester, the imposed displacement and experienced acceleration can be unknown and erratic. To reach this power target and to reduce as much as possible the volume of the harvester, a simulation canvas should be established to optimize each part of the harvester, to allow a fair comparison between different geometries and finally, to validate the entire system in its real environment. When the available space is localized and larger than a few cm³, EMEHs are often preferred to competing technologies, such as piezoelectric and electrostatic, due to their superior

yield and the already established technology and equipment for manufacturing [11]. EMEH have the major benefit of being conceptually straightforward, stemming from their close ties with widely used electromagnetic conversion systems [14]–[16]. However, when such devices are used for energy harvesting applications, the applied movement is no longer regular and periodic, which leads to tuning issues and a sub-optimal performance. Expertise from rotary electromagnetic machines has intensively been used to design and optimize harvester systems for natural linear movement [3], [16], especially for biomedical applications where the body movements are characterized by a low frequency and erratic individual patterns. Additionally, for slow imposed movement excitation of electromagnetic EHs, the efficiency is poor and the harvested energy is no longer competitive compared to other technologies such as electrostatic energy harvesters which do not rely on fast and erratic movements. Furthermore, energy harvesters are often submitted to natural accelerations that can be characterized by broad excitation frequencies [17]–[19].

Two main strategies are used to counter these problems in electromagnetic EHs. The first is to increase the gradient of the magnetic field and to reduce the step by using head-to-head permanent magnets [20]–[23]. The other one is to use a multi-stable position to trigger a fast movement once the imposed displacement is sufficiently large [24]–[27]. By combining these two approaches, one can trigger a fast oscillating movement through a rapidly changing magnetic field by applying an external slow movement to the system (for EHs which rely on a direct application of force) or by applying an external acceleration to the system (for inertial EHs). Therefore, the electromotive force (e.m.f) induced within a coil is proportional to the variation of the position with respect to time (velocity) and the variation of the magnetic flux density with respect to the position:

$$\text{e.m.f} = -N_{\text{coil}} \frac{d\phi_{\text{core}}}{dy} \frac{dy}{dt}, \quad (1)$$

where N_{coil} is the number of turns in the winding and ϕ_{core} is the average magnetic flux in the central region of the coil.

Moreover, harvesters are most often used in small areas, where the size of the EH can be considered as a constraint [4]. When the dimensions of a generator are scaled with a value S , the harvested electromagnetic energy scales with a factor between S^3 and S^4 [28]. This is due to the fact that the performance of the permanent magnets used in electromagnetic generators decreases dramatically when these are miniaturized, and the number of turns of the magnetic coils has to be reduced in order to fit the limited available space. For those reasons, accurate numerical models that predict the behavior of the system are crucial for the optimization step. Research on electromagnetic harvesters focuses on the optimization of the magnetic flux trapped by the coils [21], [29]–[32]. This work highlights the necessity of investigating

the geometry of the core to tune the resulting magnetic force in order to change and adapt the dynamics of the system and therefore its power efficiency accordingly to its environment.

The size of "small" EMEH (few tens of cm^3) proposed in the literature, remains significant and these devices are difficult to integrate in the environment for which they are designed for [33]–[36]. However, some EMEH topologies try to get around this theoretical limit by proposing innovative geometries and ways to harvest the electromagnetic energy [15], [25], [31], [37]. In a electromagnetic power generator, the mechanical and electrical parts are strongly coupled, especially for small scale EH where the harvested energy can affect the dynamics of the system. Also, due to the small quantity of energy involved, each possible loss of energy can have a significant influence onto the system. This leads to difficulties to model and compute the whole dynamics of the system but also to find optimum for a given geometry due to strongly coupled electrical and mechanical equations. One of the most important loss of energy in such a system, is the eddy currents loss due to the relative velocity between the ferromagnetic core and the magnets. Analytical solution for eddy currents are not trivial to extract for complex geometries and finite geometries with open boundaries [38]–[40]. This type of losses are often taken into account by introducing a constant damping coefficient factor extracted experimentally or estimated [7], [33], [35], [41].

This work presents a custom simulation playground to compare, optimize and predict the dynamic behavior of miniaturized axisymmetrical linear EMEH targeting wearable and biomedical applications. It also allows to derive the energy efficiency when the energy harvester is down-scaled and therefore find the optimum between size and performance for a given design geometry. The FEA simulates the magnetic induction in the ferromagnetic core as well as the magnetic flux in the coils (static mode) for each given relative position between the magnets and the ferromagnetic core. In addition, the one dimension (1D) and two degrees of freedom (2DOF) model computes the dynamics of the EH submitted to an external acceleration by introducing the coupling physics averaged over the whole geometry with a damping coefficient b_{mag} . A custom designed test bench capable of characterizing the static and dynamic modes of a linear energy harvester excited with slow and natural movements is presented in this work. This experimental approach is complemented with a generic Finite Element Analysis (FEA) to fully characterize and optimize the magnetic force in any arbitrary axisymmetric EMEHs. Dynamic experimental characterization of EMEH for wearable applications can be a complex task to achieve, and requires a dedicated and specific setup to properly characterize the harvester during its operation. A numerical approach helps to better understand the influence of each parameter and variable on the harvester and subsequently, drive the design to extract the maximum of available energy.

This paper is structured as follows. The next section describes the design and the geometry of the experimental and optimized proof of concept EH. Section III describes the custom test bench used to characterize the system and its static and dynamic modes. Section IV describes the FEA and validates the modeling results with an experimental characterization while section V describes the geometry optimization by using the FEA. Section VI describes the co-simulated numerical approach to model the mechanical and electrical behavior of the optimized system in a real environment. Finally, Section VII discussed the obtained results for a chosen set of parameters and a given external acceleration.

II. DESIGN AND GEOMETRY OF THE PROOF OF CONCEPT EMEH

An axisymmetric EMEH geometry is often chosen for manufacturing and assembly reasons. Also, to ease the machining of the ferromagnetic core from a single rod and facilitate its winding, it was decided to put the ferromagnetic core in the center surrounded by seven head-to-head ring shaped permanent magnets [20], [42]. To validate results from the FEA and set the parameters required in the simulation, a proof of concept geometry has been realized and tested with the test bench where the dimensions are given in Figure 1. This larger geometry eases the characterization of the resulting force between the magnets and the ferromagnetic core under the test bench. It also allows to determine the remanent magnetization B_r of the used magnets before the optimization and miniaturization of the geometry. The two coils are connected and the magnetic flux can flow from one coil to another, as will be discussed in Section IV.

A C45 carbon steel material has been used to manufacture the ferromagnetic core because of its low hysteresis, high saturation and its adequate machinability. Due to the machining process, the associated tolerances reach ± 0.2 mm for the length of the flanges, leading to an air gap $G = 1.5 \pm 0.2$ mm. This voluntarily large gap is used to reduce to an acceptable level the radial force occurring in practice between the fixed part and the moving part of the EH. For consistent modeling, the actual dimensions of the ferromagnetic core have been measured and used for the simulation. Also, to strongly fix the ferromagnetic core on the test bench, a thread hole was drilled at the bottom of this core which introduces a small top/bottom asymmetry, which is taken into account in the simulation. As described in Section VI, the vertical force (y -direction) between the ferromagnetic core and the magnets can be large and therefore limit the displacement of the proof-mass for inertial EHs. In this tested geometry, the single iron coil (consisting in two flanges and a winding in between) is duplicated at a distance of 4 mm to reduce magnetic force in the y -direction and so to lower the whole force acting on the system. As detailed in Section VII, this second building

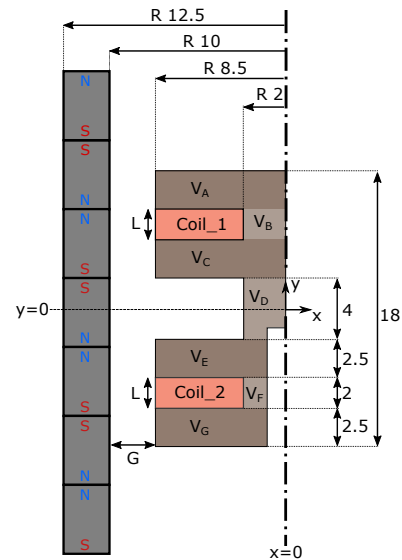


FIGURE 1. Cross section of the proof of concept EH architecture (dimensions are in mm) tested with the test bench.

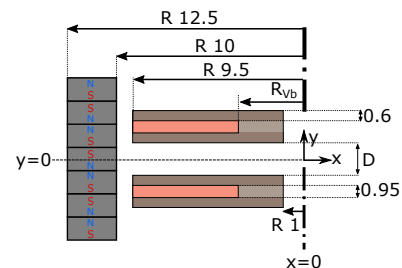


FIGURE 2. Cross section of the optimized and miniaturized EH architecture (dimensions are in mm) simulated in the 1D 2DOF model.

block allows to step through multiple stable positions when holding the magnets by a spring [24]. Duplicating the number of stable positions and reducing the peaks of the magnetic force is achieved by changing the distance between the two coils.

The moving part is chosen to be the magnet in this EMEH topology in order to fix the two coils and their interconnections with the electrical Power Management Unit (PMU). In the optimized geometry, shown in Figure 2, it was decided to miniaturize this EH to fit a volume of 10 cm^3 . The displacement range of the magnets is constrained to ± 3 mm and can go through seven different equilibrium positions (where $F_{tot} = 0$). In order to avoid the magnetic flux going from one coil to another (see Section IV), it is important to decouple the two coils to reduce the vertical force. This can be achieved by replacing the central region V_D by a non-ferromagnetic material.

III. EXPERIMENTAL SETUP

A custom test bench (Figure 3) has been designed and assembled to characterize various energy harvesting systems based on linear movement by imposing a specific slow

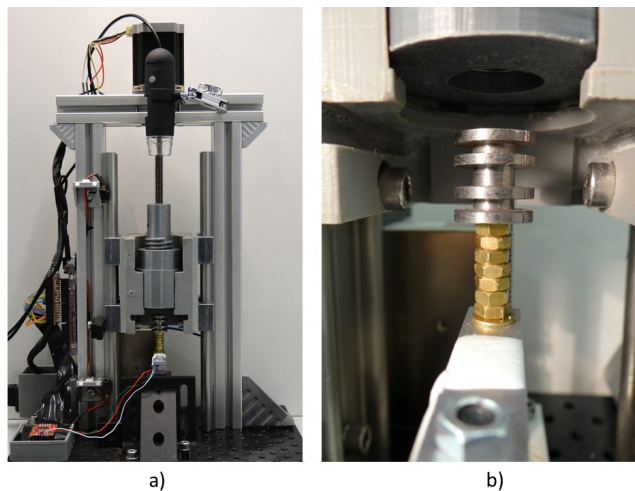


FIGURE 3. (a) Test bench. (b) A close-up view of the ferromagnetic core fixed to the load cell.

displacement up to 10 mm/s maximum speed or a specific load on which the sample can be fixed. The test bench can work statically or in a dynamic mode to characterize low frequency movements. Also, it can impose a specific force on a tested design and measure the resulting displacement (squeezed/compression or stretched/traction effect). Time, position and force are the three main variables measured during the experiment. External hardware is also used for electrical characterization and is synchronized with the movement.

The moving carriage is guided by two linear rails for accurate positioning ($5 \mu\text{m}$ resolution (no load) with a maximum displacement of 100mm along the y-axis). A lead screw (step 2mm) driven by a stepper motor (*Step-Syn*, DC 3A, 1.8 Deg) is controlled by a dedicated motor driver circuit (*ROHM-STEPMO-EVK-202*). A load cell weighing sensor (max load ± 5 kg) is connected to a 24-bit $\Delta\Sigma$ -ADC. A three core microcontroller (*TC275*) is used to drive the stepper motor, the weighing scale and the limit switches. A back-light is placed on the test bench to enable visual characterization using a camera in order to ease the positioning and allignement of the fixed part with the moving one. Finally, an external USB DAQ (*Native Instrument USB-62xx*) can be used for electrical characterization during the movement. The functionality of the test bench is controlled by using a Graphical User Interface to enable the experimental process and data capture and to guarantee repeatability over each measurement. The schematic diagram of each element composing the test bench is shown in Figure 4 and 5.

To perform dynamic measurements, parallel computing is used. The main process focuses on the communication with the microcontroller and sends instructions to the stepper motor, while receiving the values from the force sensor. The second process is dedicated to communicating with the

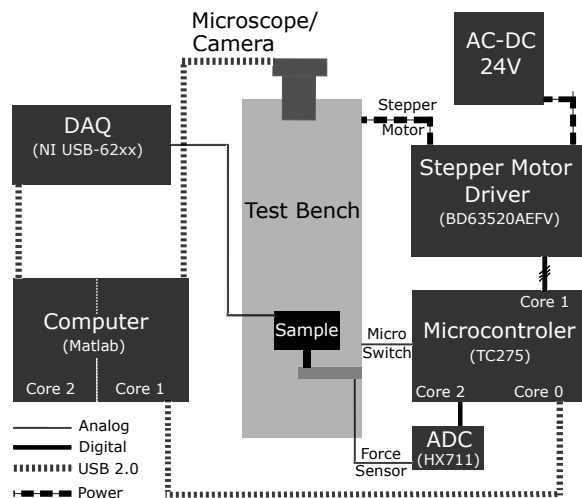


FIGURE 4. Test bench: block diagram of the integrated hardware.

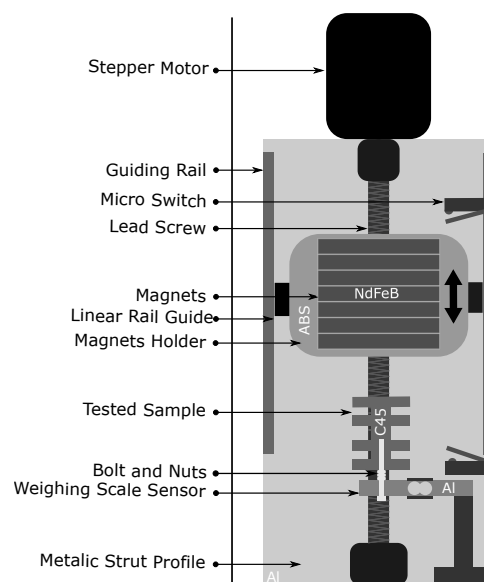


FIGURE 5. Test bench: schematic of the mechanical setup.

external hardware and to clear the buffer periodically during the experiment. The three cores in the microcontroller are used to control the communication with the software, the stepper motor and the weighing scale sensor respectively. In this way, variability in communication latency on the serial USB buses does not affect the imposed dynamic movement.

Figure 3 b) shows the ferromagnetic core fixed to the load cell. The magnets are inserted on a specific holder fixed to the main moving carriage. All parts are 3D printed in ABS and brass screws and nuts are used to avoid perturbation in the magnetic flux induction within the central core. Also, the metallic parts are kept at a controlled distance from the magnets to reduce the generation of eddy currents during the flux variation.

The load cell has been calibrated and shows a linearity smaller than 0.5% for the range [-8.5;8.5]N and an accuracy of ± 50 mg. Also, the displacement of the main carriage has been calibrated. The measurement error in the imposed position is due to mechanical slack and the mechanical deformation between the different parts (magnets holder, carriage holder, linear guide, lead screw,...). For a load smaller than 10 N, a total error in the imposed position below $20 \mu\text{m}$ was observed. It has been verified that those deviations in the experimental measurement from the test bench can be neglected in the following sections and the moving system can be considered as very stiff.

IV. FINITE ELEMENT MODEL

A finite element analysis has been developed using the open-source *GetDP* numerical solver [43] to characterize the electromagnetic force between the ferromagnetic core and the magnets by computing the Maxwell stress tensor for a generic axisymmetrical geometry. Also, the magnetic flux in the ferromagnetic core, in static mode, was extracted from the simulation leading to the magnetic damping coefficient detailed in the next section.

The magnetic force is a function of the relative displacement of the magnets to the ferromagnetic core. Depending on the magnets' configuration, the geometries of all the parts, the properties of each material and the position of the magnets, this force will be different. Using the Maxwell stress tensor T given by Eq.(2), the resulting force on each part of the system can be computed.

$$\mathbf{T} = \sigma_{ij} \equiv \underbrace{\epsilon \left(E_i E_j - \frac{1}{2} \delta_{ij} E^2 \right)}_{\sigma_E} + \underbrace{\frac{1}{\mu} \left(B_i B_j - \frac{1}{2} \delta_{ij} B^2 \right)}_{\sigma_B}, \quad (2)$$

where E is the electric field, B the magnetic flux density, δ_{ij} the Kronecker delta, ϵ the permittivity of the material and μ permeability. The force per unit volume is given by the following equation where $\mathbf{S} = \frac{1}{\mu} (\mathbf{B} \times \mathbf{E})$ stands for the Poynting's vector:

$$\mathbf{f} = \epsilon \mu \frac{\partial \mathbf{S}}{\partial t} - \nabla \cdot \sigma. \quad (3)$$

The total force on each part can be computed by integrating across each volume. Since no charge is present in air and the space charge is equal to zero in solid volumes when no relative velocity between the magnets and ferromagnetic core is present, the electric field in the empty space is equal to zero. Therefore, all the terms in Eq. (2) depending on the electric field can be removed, which drastically simplifies the expression. The force exerted on a piece of material by the other parts can be computed by an integral over the surface of the object Σ :

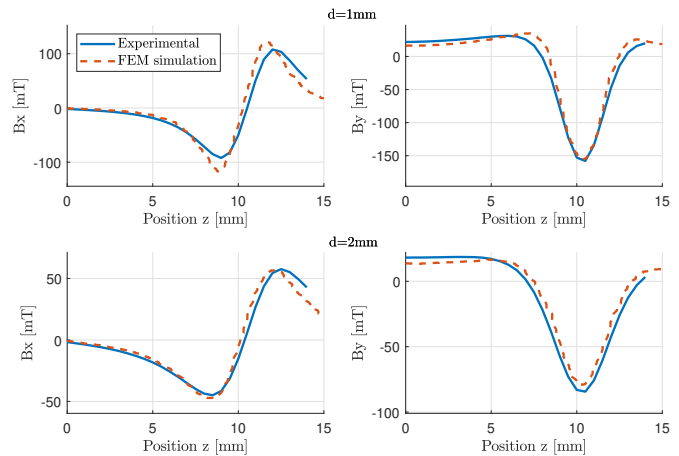


FIGURE 6. x and y components of the magnetic flux density B at two different heights from the top surface of the magnet in head-to-head configuration (grade N45). For the simulation, B_r is taken to be 1.122 T.

$$\begin{aligned} \mathbf{F}_{\text{mag}}(x, y, z) &= \oint_{\Omega} \epsilon \mu \frac{\partial \mathbf{S}}{\partial t} V + \oint_{\Sigma} \sigma \mathbf{n} \mathbf{A}, \\ \mathbf{F}_{\text{mag}}(x, y, z) &= \oint_{\Sigma} \sigma_B \mathbf{n} \mathbf{A}, \end{aligned} \quad (4)$$

where \mathbf{n} denotes the unit vector outward normal to the enclosing surface \mathbf{A} . Therefore, the force computation can be performed in post processing while knowing the established magnetic field in the whole system. For a perfect axisymmetrical design, only the y -component of the force \mathbf{F}_{mag} has to be considered (other components are equal to zero): however, this force depends on the local magnetic flux density \mathbf{B} and therefore can be different while considering saturation, hysteresis, eddy currents and Joule losses.

The B-H saturation curve has been measured directly on the carbon steel (C45) rod with a permeameter and considered for the FEA. Also, the real grade of a used magnet structure (the remanent magnetic field B_r at the surface of the magnet, used in a head-to-head configuration) has been characterized to limit as much as possible the unknowns of the simulated system. A calibrated 3-axis Hall probe sensor was used to map the magnetic flux density above the used magnet at two different distances : $d = 1$ mm and $d = 2$ mm above the upper surface of the ring magnet (mapping with a $50 \mu\text{m}$ step in x and z directions). These experimental results (solid lines in Figure 6) were compared with the finite elements simulation of a single magnet (dashed lines) and fine tuning on B_r was done accordingly. The resulting B_r of the used magnet was found to be close to $B_r = 1.122$ T and this value was considered as an input for the simulation (whereas N45 grade should be in the range of 1.32-1.37 T). There is a consistent agreement between the curves where the differences in magnetic field amplitude with respect to the z -axis are mostly due to non-uniform magnet magnetization. Also, the geometry of the real magnets is slightly

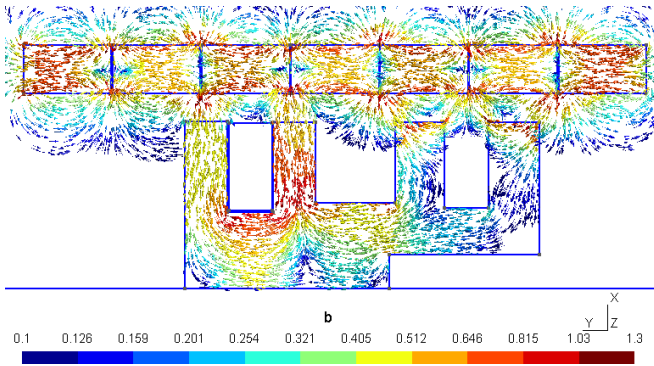


FIGURE 7. FEA on the tested geometry (Figure1): position of the ferromagnetic core at $y=-1.35$ mm.

different from a perfect hollow cylinder since the edges are chamfered leading to minor differences when compared to the simulation. The B_z measurement results in a few mT whereas the simulation, as expected, computes zero for a purely axisymmetrical geometry.

The convergence of the solution was realized on the whole structure (magnets + ferromagnetic core). The resulting force (for the position shown in Figure 7) was chosen as the studied quantity for the mesh size analysis. The resulting force is a side quantity from the magnetic field B (as described by Eq. 4) and depends on the magnetic field B over the whole mesh. Therefore, this global quantity is very sensitive and can highly fluctuate with an inappropriate mesh. Also, the magnetic field induction expands to infinity. This corresponding boundary condition is imposed by adding an external infinite domain (outer shell) for the simulation to force the vector potential to be zero at infinity. The characteristic length for the mesh was set to $60 \mu\text{m}$ for the ferromagnetic core and the magnets to ensure a satisfactory convergence of the resulting force with a deviation of ± 0.64 N. Figure 7 shows the resulting magnetic flux density in the 2D axisymmetrical system depicted in Figure 1. One can observe the resulting radial magnetic flux density escaping from the head-to-head magnets. This magnetic flux density is well captured by the flanges of the ferromagnetic core when the latter are facing the interface between the two magnets.

Figure 8 shows the resulting force as a function of the position, in static mode, between the ferromagnetic core and the magnets. There is a satisfactory agreement between the numerical simulation and the experimental results at the beginning of the entrance of the core in the magnets. A significant deviation is observed for the amplitude of the peaks when the ferromagnetic core is well inside the stack of magnets (for $y > 12$ mm). This is expected, since at this position, the alignment is no longer guaranteed due to the tilt of the ferromagnetic core that increases owing to the resulting radial force (along x and z) that comes from this misalignment (unstable position). The ferromagnetic core

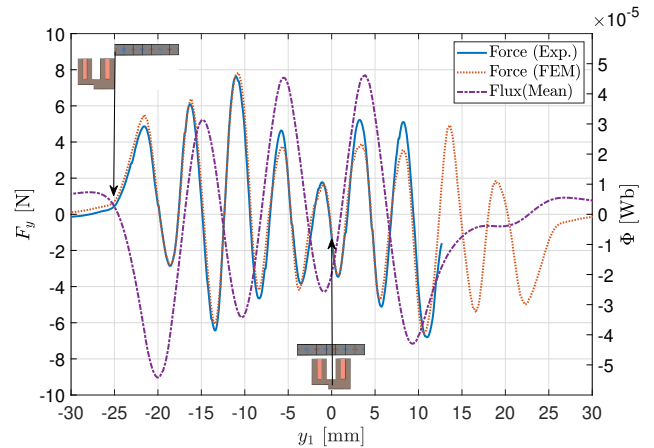


FIGURE 8. Magnetic flux in the central part of the upper coil with the superimposed resulting force (simulation and experiment) for a relative displacement between the ferromagnetic core (C45) and the magnets (N45) going from $y = -25$ mm (entrance of the core in the magnets) to $y = 12$ mm (experimental limit). Experimental (Exp.) and Simulation (FEM) curves are voluntarily aligned at $y = 0$ mm to ease the comparison. The maximum relative error between the model and the experiment in the resulting force is 44% at $y = 8.27$ mm.

bends towards the magnets, the gap G is reduced on one side, the reluctance is therefore decreased and the force increases locally. For practical reasons, the experiment had to be stopped at that point.

The magnetic flux in the central region of the upper coil is also depicted in Figure 8. Due to the axisymmetrical structure, the total flux is given by the following integral, stretching from the axisymmetrical axis ($x = 0$) to the edge of the ferromagnetic core (r):

$$\begin{aligned} \langle \phi \rangle_L &= \int_0^{2\pi} \int_0^{x=r} \langle B_y(x) \rangle_L dx d\theta, \\ \langle \phi \rangle_L &= 2\pi \int_0^{x=r} \frac{x}{n(x)} \sum_0^{y=l} B_y(x) dx d\theta, \end{aligned} \quad (5)$$

where $\langle \phi \rangle_L$ is the average flux over the height L of the coil. $n(x)$ is the number of finite elements across length L and $B_y(x)$ the y -component of the magnetic field. However, the magnetic flux is larger at the edge of the ferromagnetic core (near the coil) and much smaller inside. Therefore, as a lower bound for the magnetic flux, the average equals:

$$\langle \phi \rangle_L \approx \frac{\pi R^2}{m(y)n(x)} \sum_0^{x=r} \sum_0^{y=l} B_y(x), \quad (6)$$

where $m(y)$ is the number of finite elements across the radius R of the central part of the ferromagnetic core. The $\Delta\phi$ between two consecutive extrema is always larger than 10×10^{-5} Wb all along the path of the ferromagnetic core, whereas the resulting force between the magnets and the ferromagnetic core is divided by a factor of two when both coils are immersed in the magnets' tower.

It can be concluded that the numerical model accurately predicts the experimental observations on the resulting force,

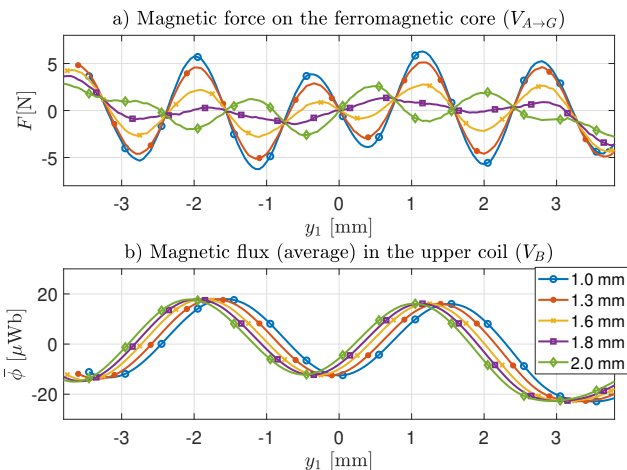


FIGURE 9. Ferromagnetic core geometry optimization: distance between the two coils D .

even for complex geometries and designs of EHs. When considering the complete system (with the spring), this force (function of the relative position between the ferromagnetic core and the magnets), can be tuned to match with the externally applied force or externally applied acceleration to the whole device in order to run through different stable positions during the movement as described in Section V.

V. OPTIMIZED EMEH DESIGN

The finite element model is used to optimize the geometry and keep $d\phi_{core}/dy$ in the central region of the coil (V_B and V_E) as large as possible. Three geometry optimizations are proposed as an example in this study. The goal is to keep the flux in each coil as large as possible while reducing the resulting vertical force. Further optimizations can be performed in the same way for various EMEH designs. In order to minimize the reluctance and therefore, increase the magnetic coupling in the coils, a first optimization has been done on the air gap G between the magnets and the flanges of the ferromagnetic core. By using the FEA presented in previous section, it was observed that the air gap should be smaller than 1.5 mm to avoid leakage fluxes. The smaller the gap, the smaller the reluctance and the larger the flux in each coil. The gap has been reduced to 500 μ m which allows an acceptable machining tolerance. A second optimization has been carried on the distance D between the two coils. The underlying idea is to counteract the magnetic force on the first coil by positioning the second coil, attached to the first one, at a distance where the force is equal in magnitude and opposed in signed to the force on the first coil. In that way the system can easily switch from one equilibrium position to another. As shown in Figure 9, the maximum resulting magnetic force can be divided by six while keeping the same $\Delta\phi$ in each coils. This leads to a maximum force of 1.3 N to overcome to switch to the next equilibrium position. Also, it is observed that all the curves cross at the same point for

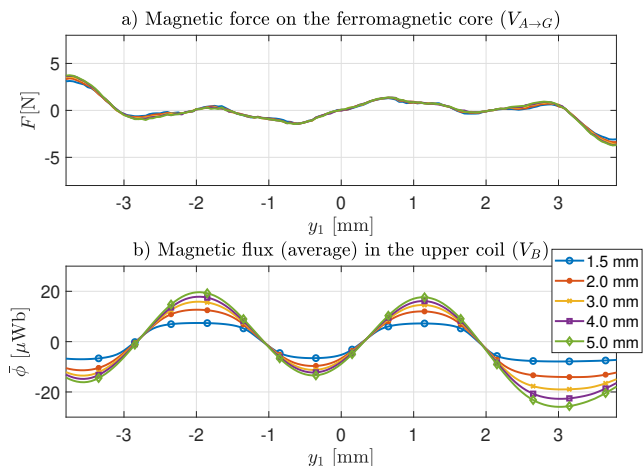


FIGURE 10. Ferromagnetic core geometry optimization: inner diameter of the coils (R_{V_B} and R_{V_F}).

all those geometries. This can be explained by the fact that the two coils are exactly the same and the spacing between the two flanges (for each coil) is the same. Therefore, when the ferromagnetic core is placed symmetrically from either side of the magnets, reducing the distance between the two coils means lowering the upper coil and rising up the lower coil by the same amount. This leaves the ferromagnetic core symmetrically placed in the magnets with a lower/larger resulting force on the first coil and a larger/lower force on the second coil respectively.

A third geometry optimization has been done on the inner radius of the coil R_{V_B} and is shown in Figure 10. Reducing this radius allows larger space for the winding (larger number of turns) but also a smaller resistance of the coil (for a given number of turn) due to the smaller diameter. On the other hand, reducing the inner diameter of the coil, and so reducing the volume V_B , leads to a higher magnetic flux density that can lead to saturation in the ferromagnetic core. One can see a decrease of $\Delta\phi$ in V_B when the diameter is reduced. The saturation is clearly visible for a radius of 1.5 mm. It was decided to set this diameter to 4 mm in order to limit the saturation and therefore keep $\Delta\phi(y)$ as large as possible. The corresponding number of turn N_{wire} for each coil that can be achieved with a chosen 60 μ m diameter wire is 1200 turns.

VI. 1D SYSTEM SIMULATION IN DYNAMIC MODE

Figure 11 represents the complete system in its real environment where the external acceleration is applied to the outer shell (second DOF). A generic 1D and 2DOF Matlab/Simulink model was used to characterize the whole system when interacting with its natural environment. The first degree of freedom gathers all the forces applied directly to the magnets and the ferromagnetic core and the second degree of freedom represent the possible interactions with its

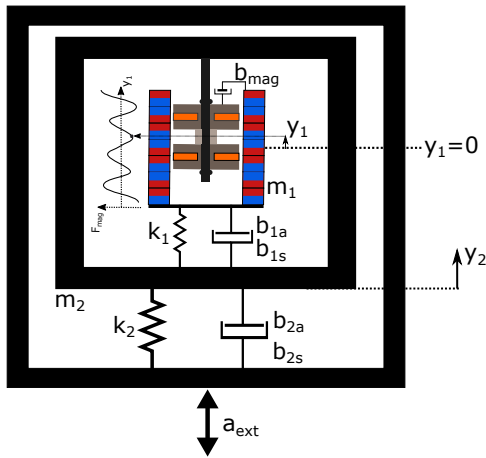


FIGURE 11. 1D 2DOF representation with the mechanical parameters interacting with the system.

holder/frame structure or an additional mass m_2 acting on the system modifying its dynamic response. The schematic of such a system is shown in Figure 12 and 13. By using the second Newton's law applied to each degree of freedom, the dynamics of the inertial system is governed by the following equations:

$$\begin{aligned} m_1 \ddot{y}_1 &= -[b_1 + b_{mag}(y_1)]\dot{y}_1 - k_1 y_1 \\ &\quad + F_{mag}(y_1) + F_{elec} - m_1 y_2, \\ m_2 \ddot{y}_2 &= b_1 \dot{y}_1 - b_2 \dot{y}_2 + k_1 y_1 - k_2 y_2 + m_2 a_{ext}, \end{aligned} \quad (7)$$

where m represents the proof-mass mass involved in the system, k the stiffness coefficient, b the damping coefficient and a_{ext} the external acceleration imposed to the second degree of freedom. The indices 1 and 2 refers to the two degrees of freedom. F_{mag} is the resulting magnetic force depending on the relative position between the magnets and the ferromagnetic core (in static mode) whereas $b_{mag}(y_1)$ is the magnetic damping coefficient resulting from eddy current losses. Finally, F_{elec} represents the force resulting from the electrical extracted energy. Each of those terms are detailed in the following section. The potential force of gravity being a constant, the system is implicitly considered in a new equilibrium state with compressed springs. Hysteresis in the ferromagnetic core is neglected as a first approximation because of the low coercivity of the C45 material used for the ferromagnetic core. The resulting block diagram of the system is represented in Figure 13, where $F_{mag}(y_1)$, $b_{mag}(y_1)$ and $\phi_{mag}(y_1)$ are interpolated from the 2D FEM simulation. When the relative motion between the coils and the magnets can be considered as small, the non-linear magnetic force can be linearized near the equilibrium position and analytical solution can be found by applying the perturbation method. To maximize the harvested energy, the displacement should be large enough to invert the magnetic flux in each coil as described in Section II.

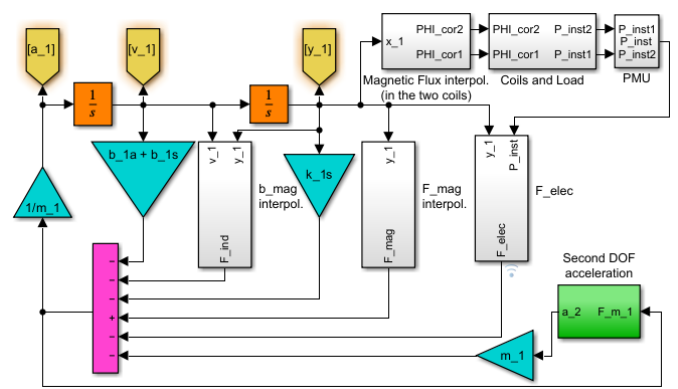


FIGURE 12. Simulink block diagram: first degree of freedom (1).

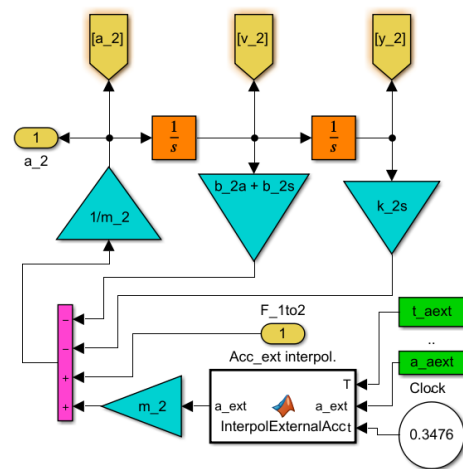


FIGURE 13. Simulink block diagram: second degree of freedom (2).

1) Mechanical damping

The first loss of mechanical energy comes from the air damping when the ferromagnetic core or the magnets oscillate at a given frequency. This term can be difficult to determine with a satisfactory accuracy due to the complex geometry of the whole structure and frame and therefore requires numerical modeling. However, a first approximation of this term can be given by a dimensional analysis. First, one must know the regime in which the moving parts are displaced in the fluid (air). The Reynolds number Re expressed in Equation (8) indicates if the system evolves in a Stokes, laminar, transient or turbulent flow.

$$Re = \frac{\rho_{air} L_c U}{\mu_{air}} \approx 620, \quad (8)$$

where L_c is a characteristic length (the inner diameter of the magnets core in our case), U the speed of the flow around the magnet set to 0.5m/s after a first analysis without damping, μ_{air} and ρ_{air} respectively the dynamic viscosity of the air and the density of the air.

This Reynold number is smaller than 1000. Therefore the regime can be assumed to be laminar and the viscous forces dominant in the drag forces compared to the pressure forces. One can use the Stokes's law to find the viscous drag forces. However, the geometry of the core is far different from a perfect sphere. Therefore, one can introduce a shape factor K [44] as shown in Eq.(9):

$$F_{drag} = 6\pi K \mu_{air} L_v U \quad (9)$$

where L_v is the radius of a sphere with the same volume as the object. This force is proportional to the velocity of the magnet (or equivalently the velocity of the flow around the fixed magnet) and therefore the air damping coefficient can be given by $b_d^{air} = 6\pi K \mu_{air} L_v$ which is in the order of 10^{-8} and therefore can be neglected compared to the other terms as will be shown in Section VI-2.

An additional type of damping that needs to be considered in those type of small EMEH is the structural damping due to dissipation of energy in the spring while its vibrating. During the deformation of the spring, a dissipation of energy takes place within the material due to internal frictions. Experimental results show that this energy E_{struct}^{loss} is proportional to the square of the displacement amplitude $|y|$. However, this term remain below 10^{-8} in magnitude in our design and can also be neglected against the magnetic damping coefficient.

2) Eddy currents

Accordingly to the Faraday's law, the variation of the flux, due to the head-to-head magnets, near the flanges will induce eddy current in the ferromagnetic core ($\sigma_{cor} \approx 4 \times 10^7$ S/m). This will cause a reduction of the magnetic flux entering in the flanges and therefore in the central region of the coil. The ferromagnetic core is a conducting material where eddy currents occur. The other parts of the EMEH are considered as non-conducting. For the magnet, the conductivity of NdFeB is one order of magnitude below the one of the C45 material and the coil is made of a thin wire ($60 \mu\text{m}$) wounded perpendicularly to the magnetic field meaning that eddy currents can be neglected in the magnets and the wire.

The losses related to the eddy current are considered by introducing a magnetic damping coefficient $b_{mag}(y_1)$ (where y_1 is the position of the ferromagnetic core relatively to the magnets) resulting in a force proportional to the relative velocity v_1 between the ferromagnetic core and the magnetic field [45]. The total force due to eddy currents can be expressed by the following integral on the total volume V_{cor} of the ferromagnetic core:

$$\mathbf{F} = \iiint_{V_{cor}} (\mathbf{j} \times \mathbf{b}) \, dV \quad (10)$$

Where $\mathbf{b}(x,y,z)$ is a non-uniform field over the structure and $\mathbf{j}(x,y,z)$ the induced current density. The latter can be expressed by using the following relation.

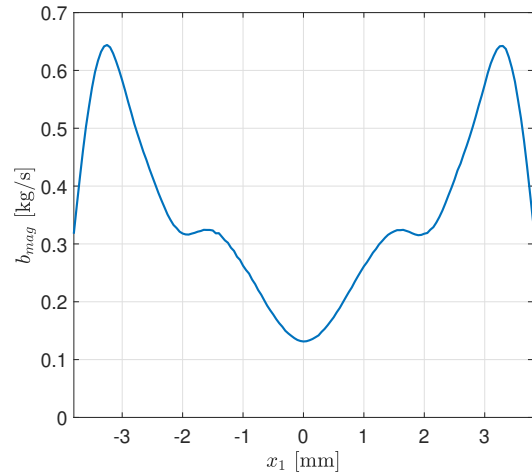


FIGURE 14. Magnetic damping coefficient b_{mag} as a function of the relative position between the magnets and the ferromagnetic core.

$$\mathbf{j} = \sigma(\mathbf{v}_1 \times \mathbf{b}) \quad (11)$$

Therefore, by considering σ_{cor} as a constant all over the core, the force exerted on the structure due to the presence of eddy currents in the ferromagnetic core is expressed as

$$\begin{aligned} \mathbf{F} &= \sigma_{cor} \iiint_{V_{cor}} (\mathbf{v}_1 \times \mathbf{b}) \times \mathbf{b} \, dV, \\ &= \sigma_{cor} \iiint_{V_{cor}} \underbrace{(\mathbf{b} \cdot \mathbf{v}_1) \mathbf{b}}_I - \underbrace{(\mathbf{b} \cdot \mathbf{b}) \mathbf{v}_1}_{II} \, dV \end{aligned} \quad (12)$$

FE analysis in Section IV shows that the axial component b_y is almost equal to zero in the volume V_A , V_C , V_E and V_G . The radial component b_x in the volume V_B , V_D and V_F is almost equal to zero due to the high permeability of the material. Therefore, only the II term of Eq.(12) can be considered for the flanges. In the central region of the core, the resulting force is equal to zero ($I+II=0$). Furthermore, in a cylindrical coordinate, $\mathbf{b}(\rho, y)$ does not depend on the angular coordinate ϕ .

$$\begin{aligned} \mathbf{F} &= -\sigma_{cor} v_1 \iiint_{V_{ACEG}} |b_x(x, y, z)|^2 \, dV \cdot \hat{y}, \\ F_y &= -v_1 \cdot \underbrace{2\pi \sigma_{cor} \iint_{V_{ACEG}} |b_\rho(\rho, y)|^2 \rho \, d\rho dy}_{b_{mag}(y_1)} \end{aligned} \quad (13)$$

$(dV = \rho d\rho d\phi dy)$

Figure 14 shows the resulting magnetic damping coefficient as a function of the relative position between the ferromagnetic core and the stack of magnets.

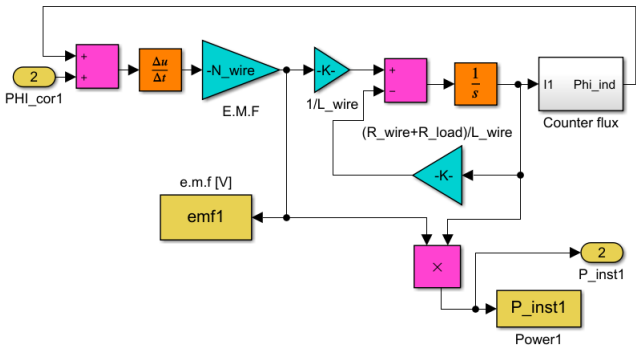


FIGURE 15. Simulink block diagram: current and voltage at the first coil.

Parameter	Value	Unit	Comments
m_1	33.6	[g]	Magnets + copper holder
m_2	100	[g]	
$k_1 s$	175	[N/m]	
$k_2 s$	520	[N/m]	For each coil
b_2	0.1	[Ns/m]	
N_{wire}	1200	[N/m]	Purely resistive
R_{wire}	285	[Ω]	
R_{load}	5000	[Ω]	

TABLE 1. Values for the parameters used in the 1D2DOF simulated system (Simulink).

and equilibrium positions as depicted in Figure 16. The spring stiffness k_1 was set to 175 N/m in order to reduce the potential barrier at $y_1 = 0$ while keeping two other stable positions at $y_1 = \pm 2.95$ mm. Both potential barriers at the extremity avoid collisions with the frame in case of large accelerations (> 40 m/s²).

The system was tested and characterized with short pulses of acceleration which corresponds to the critical situation. A 6ms pulse is generated every 2.5 s with an increased amplitude from 17.5 to 27.5 m/s². One can observe in Figure 16 the influence of the second degree of freedom to sustain the movement of the first mass m_1 but also to facilitate the system to switch from one equilibrium position to another. By using the second DOF, the system is able to go through the next equilibrium position with a smaller acceleration. The maximum theoretical power that can be extracted from each pulse in Figure 16 is depicted in Figure 17 and the stored electrical energy can be doubled by considering the 2 DOF system.

When the displacement is imposed to the first degree of freedom of the system, the energy is stored in the spring until its release when the force exerted by the spring is larger than the magnetic force. The magnets will move and stabilize to the next equilibrium position, producing a pulse of current similar to the one shown in Figure 16.

This system has also been tested under a sinusoidal external acceleration and the switching position was observed for an amplitude larger than 6.2 m/s². With an amplitude of 6.5 m/s² and a frequency of 20 Hz, the chaotic dynamics allow the system to browse each equilibrium position. The simulation shows an average RMS power of 11.2 mW. When the amplitude is set to 6 m/s², the system stabilizes around an equilibrium position and the generated power in steady state falls to 0.240 mW.

3) e.m.f and induced current

Due to the relative displacement of the coil within a non-uniform magnetic field, an electromotive force (e.m.f) will appear at the terminals of the coil accordingly to Lenz's law described by Eq. (1). If a load is connected at the terminals of the coil, a current will be induced in the latter generating a magnetic flux counteracting the main flux in the central region of the coil (V_B and V_F). Figure 15 shows the block diagram of the coil close to a resistive load where the induced-flux is considered.

This analysis considers that the signal is perfectly rectified and conditioned with a Power Management Unit (PMU) with no associated losses. This approach allows to focus on the theoretical limit of the design without being influenced by the way the energy is captured and stored. However, the induced flux of the two coils closed on a resistive load reduces the overall magnetic field in the ferromagnetic core and therefore the force acting on the magnets is modified accordingly. The force F_{elec} is added to the system to take into account the extracted electrical energy from the EH. This force is proportional to the e.m.f and therefore to the square of the relative velocity between the magnets and the ferromagnetic core following Eq.(1).

VII. RESULTS AND DISCUSSION

In this section, the system is submitted to short pulses external acceleration. The position, velocity and acceleration of each degree of freedom is recorded as well as the generated voltage and current, and therefore the maximum generated power from both coils. Table 1 lists all the fixed parameters used for all the simulations of the proposed design.

The mass and spring stiffness of the second DOF are fixed according to the resonant frequency of the first DOF. In this way, the oscillation of the mass m_2 keeps the movement of the first mass m_1 (magnets) and therefore produces the maximum energy. From the force exerted by the spring k_1 and the force exerted by the magnets onto the ferromagnetic core, a potential diagram can be extracted to highlight stable

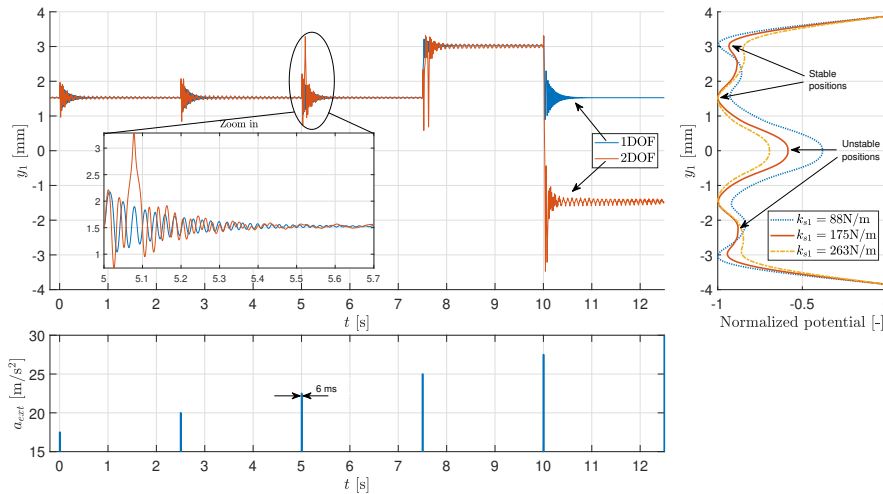


FIGURE 16. Simulation of the dynamic response (y_1) of the 1D linear EMEH (optimized geometry) submitted to increasing short pulses external acceleration (a_{ext}).

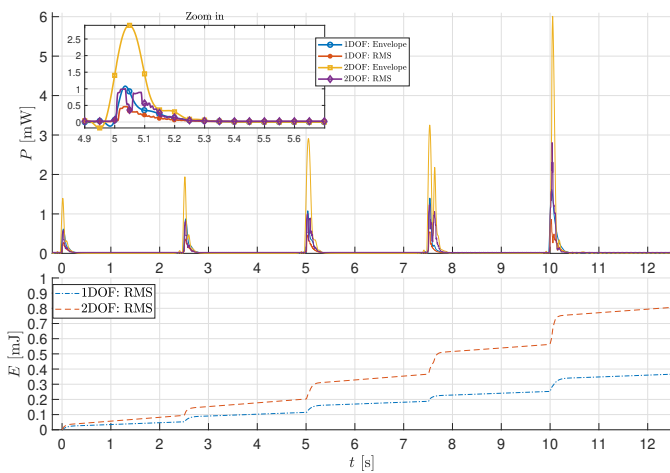


FIGURE 17. Generated power of the 1D linear EMEH (optimized geometry) for the external acceleration (a_{ext}) given in Figure 16.

VIII. CONCLUSION

This paper presents a complete experimental test bench and simulation environment to design and optimize miniaturized linear axisymmetric EMEHs targeting wearable and bio-implantable systems. An optimized design with a double coil is proposed to reduce the magnetic force. Head-to-head permanent ring magnets were used to generate a radial magnetic field with a large gradient in the y -direction. To ease the understanding of the system and its behavior, two identical coils have been considered. More complex geometries comprising multiple coils as well as inner/outer coils, and other hybrid combinations, can be considered to further reduce the volume, change the aspect ratio (as a function of the desired geometrical form factor) and maximize the produced

energy. A custom test bench characterizes multiple energy harvesters, especially small EMEHs. A Finite Element Analysis (FEA) measuring miniaturized EHs was used to optimize the geometry of the ferromagnetic core and numerical results show a good agreement with the experimental results obtained with the test bench. The model was built to test different geometries and optimize the system: any geometry of ferromagnetic cores and magnets can be loaded in the system, with an access to the required design parameters for the simulation in order to work through the comparison and the optimization step. By using the double coil structure, it has been demonstrated that the intensity of the magnetic flux going through the flanges can be kept to its highest value while significantly reducing the resulting magnetic force. This optimization allows a crucial tuning in order to step through multiple stable positions during the excitation of EH systems using the principle of inertial masses or when a slow displacement is imposed to the second DOF. The proposed design shows a dynamic response to short acceleration pulses (6 ms) smaller than 3 g with a maximum theoretical power of 1 mW during 150 ms. Additional work should be done to characterize in detail the proposed multi-stable system with its associated PMU.

ACKNOWLEDGMENT

The research has been partially carried out in the work of the SWS project. This project is supported by the Walloon Region of Belgium (pole Mecatech – convention 7278) and is carried out by a consortium of research institutions and companies. The authors would like to thank J.-F. Fagnard and his research lab (*Measurements and Instrumentation laboratory*) for the collaboration on magnetic characterization.

REFERENCES

- [1] J. H. Kim, Y. J. Shin, Y. D. Chun, and J. H. Kim, "Design of 100W Regenerative Vehicle Suspension to Harvest Energy from Road Surfaces," *International Journal of Precision Engineering and Manufacturing*, vol. 19, pp. 1089–1096, jul 2018.
- [2] H. J. Jung, I. H. Kim, and S. J. Jang, "An energy harvesting system using the wind-induced vibration of a stay cable for powering a wireless sensor node," *Smart Materials and Structures*, vol. 20, jul 2011.
- [3] W. Li, K. T. Chau, and J. Z. Jiang, "Application of linear magnetic gears for pseudo-direct-drive oceanic wave energy harvesting," in *IEEE Transactions on Magnetics*, vol. 47, pp. 2624–2627, oct 2011.
- [4] P. D. Mitcheson, E. M. Yeatman, G. K. Rao, A. S. Holmes, and T. C. Green, "Energy harvesting from human and machine motion for wireless electronic devices," *Proceedings of the IEEE*, 2008.
- [5] G. Colson, P. Laurent, P. Bellier, S. Stoukatch, F. Dupont, and M. Kraft, 2017 IEEE 14th International Conference on Wearable and Implantable Body Sensor Networks (BSN) : 9-12 May 2017. *IEEE Engineering in Medicine and Biology*, 2017.
- [6] H. C. Baelhadj, S. S. Adhikari, H. Davoodi, V. Badilita, and M. Beyaz, "A sub-cm3 energy harvester for in-vivo biosensors," *Microelectronic Engineering*, p. 111288, mar 2020.
- [7] M. Geisler, S. Boisseau, M. Perez, P. Gasnier, J. Willemin, I. Ait-Ali, and S. Perraud, "Human-motion energy harvester for autonomous body area sensors," *Smart Materials and Structures*, vol. 26, feb 2017.
- [8] N. G. Elvin and A. A. Elvin, "Vibrational energy harvesting from human gait," *IEEE/ASME Transactions on Mechatronics*, vol. 18, no. 2, pp. 637–644, 2013.
- [9] A. Zurbuchen, A. Haeberlin, A. Pfenniger, L. Bereuter, J. Schaefer, F. Jutzi, C. Huber, J. Fuhrer, and R. Vogel, "Towards Batteryless Cardiac Implantable Electronic Devices - The Swiss Way," *IEEE Transactions on Biomedical Circuits and Systems*, vol. 11, pp. 78–86, feb 2017.
- [10] A. Nasiri, S. A. Zabalawi, and D. C. Jetter, "A linear permanent magnet generator for powering implanted electronic devices," *IEEE Transactions on Power Electronics*, vol. 26, no. 1, pp. 192–199, 2011.
- [11] X. Tang, X. Wang, R. Cattley, F. Gu, and A. D. Ball, "Energy Harvesting Technologies for Achieving Self-Powered Wireless Sensor Networks in Machine Condition Monitoring: A Review," *Sensors (Basel, Switzerland)*, vol. 18, no. 12, 2018.
- [12] X. Huang, L. Wang, H. Wang, B. Zhang, X. Wang, R. Y. Stening, X. Sheng, and L. Yin, "Materials Strategies and Device Architectures of Emerging Power Supply Devices for Implantable Bioelectronics," apr 2020.
- [13] S. Kumari, S. S. Sahu, B. Gupta, and S. Kumar Mishra, "Energy harvesting via human body activities," in *Smart Biosensors in Medical Care*, pp. 87–106, Elsevier, 2020.
- [14] G. Qiyu, S. Ming, L. Huicong, M. Xin, C. Zhaohui, C. Tao, and S. Lining, "Design and experiment of an electromagnetic ocean wave energy harvesting device,"
- [15] J. M. Kim, M. M. Koo, J. H. Jeong, K. Hong, I. H. Cho, and J. Y. Choi, "Design and analysis of tubular permanent magnet linear generator for small-scale wave energy converter," *AIP Advances*, vol. 7, may 2017.
- [16] Stamenkovic, I. and Milivojevic, N. and Zheng, C. and Khaligh, A., "Three Phase Linear Permanent Magnet Energy Scavenger Based on Foot Horizontal Motion," *Twenty-Fifth Annual IEEE Applied Power Electronics Conference and Exposition (APEC)*, 2010.
- [17] S. D. Kwon, J. Park, and K. Law, "Electromagnetic energy harvester with repulsively stacked multilayer magnets for low frequency vibrations," *Smart Materials and Structures*, vol. 22, may 2013.
- [18] C. Wei and X. Jing, "A comprehensive review on vibration energy harvesting: Modelling and realization," *Renewable and Sustainable Energy Reviews*, 2017.
- [19] Y. Zhang, T. Wang, A. Luo, Y. Hu, X. Li, and F. Wang, "Micro electrostatic energy harvester with both broad bandwidth and high normalized power density," *Applied Energy*, 2018.
- [20] C. Cepnik, O. Radler, S. Rosenbaum, T. Ströhl, and U. Wallrabe, "Effective optimization of electromagnetic energy harvesters through direct computation of the electromagnetic coupling," *Sensors and Actuators, A: Physical*, vol. 167, pp. 416–421, jun 2011.
- [21] L. Zuo, B. Scully, J. Shestani, and Y. Zhou, "Design and characterization of an electromagnetic energy harvester for vehicle suspensions," *Smart Materials and Structures*, vol. 19, no. 4, 2010.
- [22] C. Blache and G. Lemarquand, "New Structures For Linear Displacement Sensor With High Magnetic Field Gradient," *IEEE Transactions on Magnetics*, vol. 28, 1992.
- [23] M. Duffy and D. Carroll, "Electromagnetic generators for power harvesting," *35th Annual IEEE Power Electronics Specialists Conference*, 2004.
- [24] M. Gao, Y. Wang, Y. Wang, and P. Wang, "Experimental investigation of non-linear multi-stable electromagnetic-induction energy harvesting mechanism by magnetic levitation oscillation," *Applied Energy*, vol. 220, pp. 856–875, jun 2018.
- [25] H. Nguyen and H. Bardaweel, "Multi-stable magnetic spring-based energy harvester subjected to harmonic excitation: comparative study and experimental evaluation," *International Mechanical Engineering Congress and Exposition IMECE2018*, nov 2018.
- [26] Z. Wu, R. L. Harnes, and K. W. Wang, "Energy Harvester Synthesis Via Coupled Linear-Bistable System With Multistable Dynamics," *Journal of Applied Mechanics*, 2014.
- [27] A. Cammarano, S. G. Burrow, and D. A. Barton, "Modelling and experimental characterization of an energy harvester with bi-stable compliance characteristics," *Proceedings of the Institution of Mechanical Engineers. Part I: Journal of Systems and Control Engineering*, vol. 225, pp. 475–484, jun 2011.
- [28] W. S. Trimmer, "Microrobots and micromechanical systems," *Micromechanics and MEMS: Classic and Seminal Papers to 1990*, vol. 19, pp. 96–116, 1997.
- [29] A. Zurbuchen, A. Haeberlin, L. Bereuter, A. Pfenniger, S. Bosshard, M. Kernen, P. Philipp Heinisch, J. Fuhrer, and R. Vogel, "Endocardial energy harvesting by electromagnetic induction," *IEEE Transactions on Biomedical Engineering*, vol. 65, pp. 424–430, feb 2018.
- [30] Z. Wang, C. Huber, J. Hu, J. He, D. Suess, and S. X. Wang, "An electrodynamic energy harvester with a 3D printed magnet and optimized topology," *Applied Physics Letters*, vol. 114, jan 2019.
- [31] K. Fan, Y. Zhang, H. Liu, M. Cai, and Q. Tan, "A nonlinear two-degree-of-freedom electromagnetic energy harvester for ultra-low frequency vibrations and human body motions," *Renewable Energy*, vol. 138, pp. 292–302, aug 2019.
- [32] G. Aldawood, H. T. Nguyen, and H. Bardaweel, "High power density spring-assisted nonlinear electromagnetic vibration energy harvester for low base-accelerations," *Applied Energy*, vol. 253, nov 2019.
- [33] C. Li, S. Wu, P. C. K. Luk, M. Gu, and Z. Jiao, "Enhanced bandwidth nonlinear resonance electromagnetic human motion energy harvester using magnetic springs and ferrofluid," *IEEE/ASME Transactions on Mechatronics*, vol. 24, pp. 710–717, apr 2019.
- [34] Y. M. Choi, M. G. Lee, and Y. Jeon, "Wearable biomechanical energy harvesting technologies," 2017.
- [35] K. Ylli, D. Hoffmann, A. Willmann, P. Becker, B. Folkmer, and Y. Manoli, "Energy harvesting from human motion: Exploiting swing and shock excitations," *Smart Materials and Structures*, vol. 24, feb 2015.
- [36] S. P. Beeby, M. J. Tudor, and N. M. White, "Energy harvesting vibration sources for microsystems applications," *Measurement Science and Technology*, 2006.
- [37] M. Gao, Y. Wang, Y. Wang, and P. Wang, "Experimental investigation of non-linear multi-stable electromagnetic-induction energy harvesting mechanism by magnetic levitation oscillation," *Applied Energy*, vol. 220, pp. 856–875, jun 2018.
- [38] A. A. Kolyshekin, "Solution of Direct Eddy Current Problems with Cylindrical Symmetry," 2013.
- [39] G. Sinha and S. S. Prabhu, "Analytical model for estimation of eddy current and power loss in conducting plate and its application," *Physical Review Special Topics - Accelerators and Beams*, vol. 14, jun 2011.
- [40] K. Weise, M. Carlstedt, M. Ziolkowski, H. Brauer, and H. Toepfer, "Lorentz Force on Permanent Magnet Rings by Moving Electrical Conductors," *IEEE Transactions on Magnetics*, vol. 51, dec 2015.
- [41] D. F. Berdy, D. J. Valentino, and D. Peroulis, "Kinetic energy harvesting from human walking and running using a magnetic levitation energy harvester," *Sensors and Actuators, A: Physical*, 2015.
- [42] J. Kravčák, "Optimization of magnetic flux in electromagnetic vibrating generators," *Trans Motauto World*, 2017.
- [43] P. Dular and C. Geuzaine, "GetDP reference manual: the documentation for GetDP, a general environment for the treatment of discrete problems." <http://getdp.info>.
- [44] D. Leith, "Drag on nonspherical objects," *Aerosol Science and Technology*, 1987.
- [45] B. Ebrahimi, M. B. Khamesee, and F. Golnaraghi, "Eddy current damper feasibility in automobile suspension: modeling, simulation and testing," *Smart Materials and Structures*, vol. 18, p. 015017, jan 2009.



G. DIGREGORIO was born in Liège, Belgium in 1994. He received a bachelor's degree from the Faculty of applied sciences, University of Liège, in 2016. He received a master's degree in engineering physics at the University of Liège in 2018. His research interests include microfluidics, electromagnetics, modeling and simulation in the field of energy harvesting.



H. PIERRE was born in Liège, Belgium in 1993. He received a bachelor's degree in applied engineering from Helmo Gramme in 2014. He received a bachelor's degree from the Faculty of applied sciences, University of Liège, in 2015. He received a master's degree in biomedical engineering at the University of Liège in 2017. His research interests include analog and digital electronics, RF engineering and bioelectronics.



P. LAURENT graduated from the University of Liège (Belgium) in 2002 as an electromechanical engineer. Then, he did his PhD on measurement and instrumentation, focusing on thermal effects in superconductors. After, he worked as Materials and Process Engineer in aeronautics at Safran Aero Booster. He then returned to the University of Liège (2010) as a research engineer at the Microsys Lab. In March 2016, he was part of the team won the \$1 million prize for the Little Box

Challenge, an engineering competition run by Google and the IEEE's Power Electronics Society. In June 2016, he won first prize at the 5G World 2016 Innovation Accelerator (London). Currently, Philippe LAURENT is doing research in Ultra-Low-Power IoT.



J.-M. REDOUTÉ (M'09-SM'12) received the degree of M.S. in electronics at the University College in Antwerp (1998), and the degree of M.Eng. in electrical engineering at the University of Brussels (2001). In August 2001, he started working at Alcatel Bell in Antwerp, where he was involved in the design of analog microelectronic circuits for telecommunications systems. In January 2005, he joined the University of Leuven as a Ph. D. research assistant. In May 2009, he defended his

Ph. D. entitled "Design of EMI resisting analog integrated circuits". In September 2009, he started working at the Berkeley Wireless Research Center at the University of California, at Berkeley: this research was funded by the Belgian American Educational Foundation (BAEF). In September 2010, he joined Monash University, Melbourne, as a senior lecturer. In July 2018, he started working at the University of Liège as an Associate Professor. His research is concentrated on miniaturized and low-power sensor interfaces, robust mixed-signal integrated circuit (IC) design with a high immunity to electromagnetic interference (EMI), biomedical (integrated and non-integrated) circuit design, energy harvesting and integrated imagers. Jean-Michel Redouté is an Associate Editor of the IEEE Sensors Journal.

• • •